RSC Advances

PAPER

View Article Online
View Journal | View Issue



Cite this: *RSC Adv.*, 2021, **11**, 5874

# Mechanochemical synthesis of pure phase mixed-cation/anion $(FAPbI_3)_x(MAPbBr_3)_{1-x}$ hybrid perovskite materials: compositional engineering and photovoltaic performance†

Sheng Tang,‡[a] Xinyu Xiao,‡[a] Jing Hu,[a] Bo Gao,[a] Hunglin Chen,[a] Zhuang Zuo,[a] Qi Qi,[a] Zongyang Peng,[a] Jianchun Wen[a] and Dechun Zou *[ab]

Organic–inorganic hybrid perovskites have emerged as promising light harvesting materials for many optoelectronic devices. Here, we present a facile mechanochemical synthesis (MCS) route for the preparation of a series of pure phase mixed-cation/anion $(FAPbI_3)_x(MAPbBr_3)_{1-x}$ ($0 \leq x \leq 1$) hybrid perovskite materials for high-efficiency thin-film perovskite solar cells (PSCs). The use of $(\alpha\text{-}FAPbI_3)_{0.95}(MAPbBr_3)_{0.05}$ perovskite prepared by MCS for the thin-film PSCs achieves a maximum PCE of 15.9% from a current–voltage ($J$–$V$) scan, which stabilises at 15.4% after 120 s of the maximum power point output. Furthermore, PSCs based on $(KPbI_3)_{0.05}(FAPbI_3)_{0.9}(MAPbBr_3)_{0.05}$ perovskite prepared by MCS exhibit higher photovoltaic performance and lower hysteresis compared with $(\alpha\text{-}FAPbI_3)_{0.95}(MAPbBr_3)_{0.05}$, with a maximum PCE of 16.7%. These results indicate that the use of mechanochemically synthesised perovskites provides a promising strategy for high performance PSCs and superior control in optoelectronic properties, leading to improved control in fabrication approaches and facilitating the development of efficient and stable PSCs in the future.

Received 22nd December 2020
Accepted 18th January 2021

DOI: 10.1039/d0ra10751d

rsc.li/rsc-advances



## Introduction

Organic–inorganic hybrid perovskite materials have the advantages of high light absorption coefficient, high balanced hole and electron mobility, long carrier lifetime, low trap-state density and excellent photovoltaic performance.[1–8] Recently, extensive research has been carried out on hybrid perovskite materials and devices in the formation of solution-processed films, solvent engineering, defect engineering and energy band engineering.[1,9–18] The maximum power conversion efficiency (PCE) of perovskite solar cells (PSCs) has exceeded 25%, which is comparable to those of polycrystalline Si, CdTe and CIGS solar cells.[19]

Recent studies of PSCs indicated that the composition of hybrid perovskites is recognised as one of the important factors in improving the photovoltaic performance. We have recently showed that engineering the halide anion composition (for example, replacing I with Br) of $MAPbI_3$ ($MA = CH_3NH_3$) can tune the bandgaps from 1.5 eV to 2.3 eV by incorporating $MAPbBr_3$ and resulted in colour tunability.[20] With regard to the organic cation MA, the mixing of formamidinium (FA) extended the absorption edge from 800 nm to 850 nm.[21,22] We expect that this reduced bandgap may allow light absorption over a broad solar spectrum, and the photocurrent of PSCs could be increased. However, the pure $FAPbI_3$ contains a nonperovskite yellow phase ($\delta$-$FAPbI_3$), which results in low PCE of PSCs. In addition, the photoactive black phase of $FAPbI_3$ ($\alpha$-$FAPbI_3$) is thermodynamically stable only above 150 °C and converts to an undesirable $\delta$-$FAPbI_3$ in an ambient atmosphere.[10,22,23] Considering their suitable bandgap (lower than $MAPbI_3$), the performance of $FAPbI_3$ solar cells can be considerably improved by stabilising the $\alpha$-$FAPbI_3$ phase. In this regard, Grätzel *et al.*[24] demonstrated an improved PCE by using mixed-cation hybrid perovskites by gradually substituting FA with MA cations. The UV-vis absorption edge of the compositional $(MA)_{0.25}(FA)_{0.75}PbI_3$ perovskite film is red-shifted from 780 nm to 830 nm compared with that of $MAPbI_3$, allowing for a higher current density. Seok *et al.*[9] have also reported a 16.2% certified PCE obtained from the $MAPb(I_{1-x}Br_x)_3$ ($x = 0.1$–$0.15$) perovskite with an extremely uniform and dense upper perovskite layer obtained by solvent engineering, whilst the absorption edge is below 770 nm. A strategy for extending the absorption range is to replace $MAPbI_3$ with $FAPbI_3$ in the $MAPb(I_{1-x}Br_x)_3$

[a]*Beijing National Laboratory for Molecular Sciences, Key Laboratory of Polymer Chemistry and Physics of Ministry of Education, Center for Soft Matter Science and Engineering, College of Chemistry and Molecular Engineering, Peking University, Beijing 100871, China. E-mail: dczou@pku.edu.cn*

[b]*Beijing Engineering Research Center for Active Matrix Display, Peking University, Beijing 100871, China*

† Electronic supplementary information (ESI) available. See DOI: 10.1039/d0ra10751d

‡ These authors contributed equally to this work.

perovskites. The incorporation of caesium cations ($Cs^+$) into the A-site of perovskite inhibited the creation of the δ-phase of $FAPbI_3$, which considerably promoted the stability of the perovskite and the reproducibility of PSCs.[25–27] Recently, the incorporation of potassium cations ($K^+$) into the A-site of the perovskite promoted the PCE to more than 20% and reduced *I–V* hysteresis of PSCs that causes uncertainty to its real PCE.[18,28] These results suggest that the composition tuning of hybrid perovskites is important to significantly improve the photovoltaic performance of PSCs and diminish *I–V* hysteresis. However, the processing parameters are now difficult to control during the thin film formation, which leads to poor repeatability.

Although solution methods are commonly used for the synthesis of hybrid perovskites, other simple, highly efficient and reproducible methods for the preparation of hybrid perovskites still exist. As recently reported for single halide perovskites prepared using a mechanochemical synthesis (MCS) approach,[24,29–34] the mechanochemically synthesised poly-crystalline $MAPbI_3$ powder was used to fabricate PSCs *via* a one-step deposition method and showed superior photovoltaic performance compared with the standard solution method. MCS of perovskites has been reported not only for ternary halide perovskites but also for a variety of compositions, including mixed perovskites that have been expanded into other A-sites (MA, FA and Cs),[35–37] B-sites (such as Sn[38,39]) and X-sites (Cl, Br and I).[40–42] All these perovskites were mechanochemically synthesised by either ball milling (BM) a mixture of AX and $PbX_2$ or BM and manually grinding a mixture of two single-halide perovskites.[43,44] To the best of our knowledge, the preparation of a systematic series of pure phase mixed-cation/anion $(FAPbI_3)_x(MAPbBr_3)_{1-x}$ perovskites by mechanochemically synthesising a mixture of $FAPbI_3$ and $MAPbBr_3$ has not been reported to date.

Following our research interest in MCS, herein we report the stabilisation of the α-$FAPbI_3$ perovskite at room temperature (RT) achieved by MCS through fine and controllable compositional engineering in pure phase mixed-cation/anion $(FAPbI_3)_x(MAPbBr_3)_{1-x}$ perovskites. The newly synthesised material was used for fabrication of PSCs by a facile one-step antisolvent method, and the device showed superior photovoltaic performance compared with a conventional solution-processed device. Furthermore, we explored the feasibility of incorporating $K^+$ into the perovskites. These results revealed that incorporating a small amount of $K^+$ into the mixed-cation/anion $(FAPbI_3)_{0.95}(MAPbBr_3)_{0.05}$ perovskite absorber significantly improved the photovoltaic performance of PSCs, and $K^+$ incorporation diminished *I–V* hysteresis.

## Results and discussion

In Fig. S1,† the yellow, black and orange powders correspond to $FAPbI_3$ (δ-phase), $FAPbI_3$ (α-phase) and $MAPbBr_3$, respectively (refer to the Experimental section for the experimental details). The mechanical-prepared yellow δ-$FAPbI_3$ powder shows a non-perovskite phase and is converted to the black perovskite phase after being annealed at 160 °C for 60 min. The α-$FAPbI_3$ powder remains in the black perovskite phase after being stored in air for 7 days, which shows good thermal stability (Fig. S2, ESI†). The mixed-cation/anion $(FAPbI_3)_x(MAPbBr_3)_{1-x}$ perovskites were prepared by mechanical BM, starting with their respective parent perovskites (Experimental section). In each series, 11 perovskites ($x = 0, 0.1, \ldots, 0.9, 1$) were synthesised. The structural and optical properties of the perovskite materials were precisely measured in detail.

Fig. 1a exhibits the XRD patterns in the $2\theta$ range of 10°–60° for $(\alpha\text{-}FAPbI_3)_x(MAPbBr_3)_{1-x}$ ($0 \leq x \leq 1$) powders prepared by MCS. Systematic shifts toward lower $2\theta$ degrees (such as (100) and (200) peaks) were observed with the increase in the α-$FAPbI_3$ content because the gradual substitution of the smaller Br atoms and MA ions with the large I atoms and FA ions increases the lattice spacing. We also prepared $(\alpha\text{-}FAPbI_3)_x(\text{-}MAPbBr_3)_{1-x}$ films *via* a wet chemical route for comparison. Fig. 1b shows the XRD patterns of the $(\alpha\text{-}FAPbI_3)_x(MAPbBr_3)_{1-x}$ films on the mp-$TiO_2$/bl-$TiO_2$/FTO substrates prepared by solvent synthesis (SS). Phase segregation was observed in the $x$ range of 0.9–1.0. The residual impurities (peaks circled in Fig. 1b) belong to δ-$FAPbI_3$ ($2\theta$, ~11.6°) and $PbI_2$ ($2\theta$, ~12.7°), and the reflection of FTO substrates are labelled in Fig. 1b. In addition, all perovskites consist of a single phase that adopts the cubic structure. Only the relative intensities of the XRD peaks of perovskites synthesised through different routes are slightly different because of the changes in their crystal orientation.

To study the optical properties in $(\alpha\text{-}FAPbI_3)_x(MAPbBr_3)_{1-x}$, we measured the UV-vis absorption spectra of powders and films. In Fig. 1c, the onset absorption band of $(\alpha\text{-}FAPbI_3)_x(\text{-}MAPbBr_3)_{1-x}$ powders can be tuned from 563 nm (2.21 eV) to 861 nm (1.44 eV), resulting in colour tunability. All spectra show clear band edge cut-offs without excitonic signature or absorption tails. Fig. 1e shows the corresponding colours of $(\alpha\text{-}FAPbI_3)_x(MAPbBr_3)_{1-x}$ powders. We can tune the colours from bright orange for $MAPbBr_3$ ($x = 0$) to brown/red for $(\alpha\text{-}FAPbI_3)_x(MAPbBr_3)_{1-x}$ and then to black for α-$FAPbI_3$ ($x = 1$) with increasing $x$ ratio through compositional control. A systematic shift in the absorption band edge to a longer wavelength with increasing α-$FAPbI_3$ content in $(\alpha\text{-}FAPbI_3)_x(\text{-}MAPbBr_3)_{1-x}$ indicates that the band gap energy ($E_g$) can be tuned by changing the composition of the perovskites. The variation of $E_g$ (estimated from the onset absorption band) with α-$FAPbI_3$ content is plotted in Fig. 1g. The nonlinear variation of $E_g$ with a composition can be expressed by following quadratic equation: $E_g((\alpha\text{-}FAPbI_3)_x(MAPbBr_3)_{1-x}) = E_g[MAPbBr_3] + (E_g[\alpha\text{-}FAPbI_3] - E_g[MAPbBr_3] - b)x + bx^2$, where $E_g(x)$ is the band gap, $x$ denotes the composition, and $b$ is the bowing parameter.[45] A least-squares fit (red line) of $E_g$ in Fig. 1g transforms the equation into $E_g(x) = 2.19 - 1.14x + 0.41x^2$, which yields the bowing parameter of $b = 0.41$ eV. The extent of bowing is a measure of the degree of fluctuations in the crystal field or the nonlinear effect arising from the anisotropic nature of binding.[46] The relatively small bowing parameter indicates that it has a good miscibility. This finding confirms that $(\alpha\text{-}FAPbI_3)_x(MAPbBr_3)_{1-x}$ primarily forms the compound and consequently enables convenient band gap tailoring by a simple MCS process.

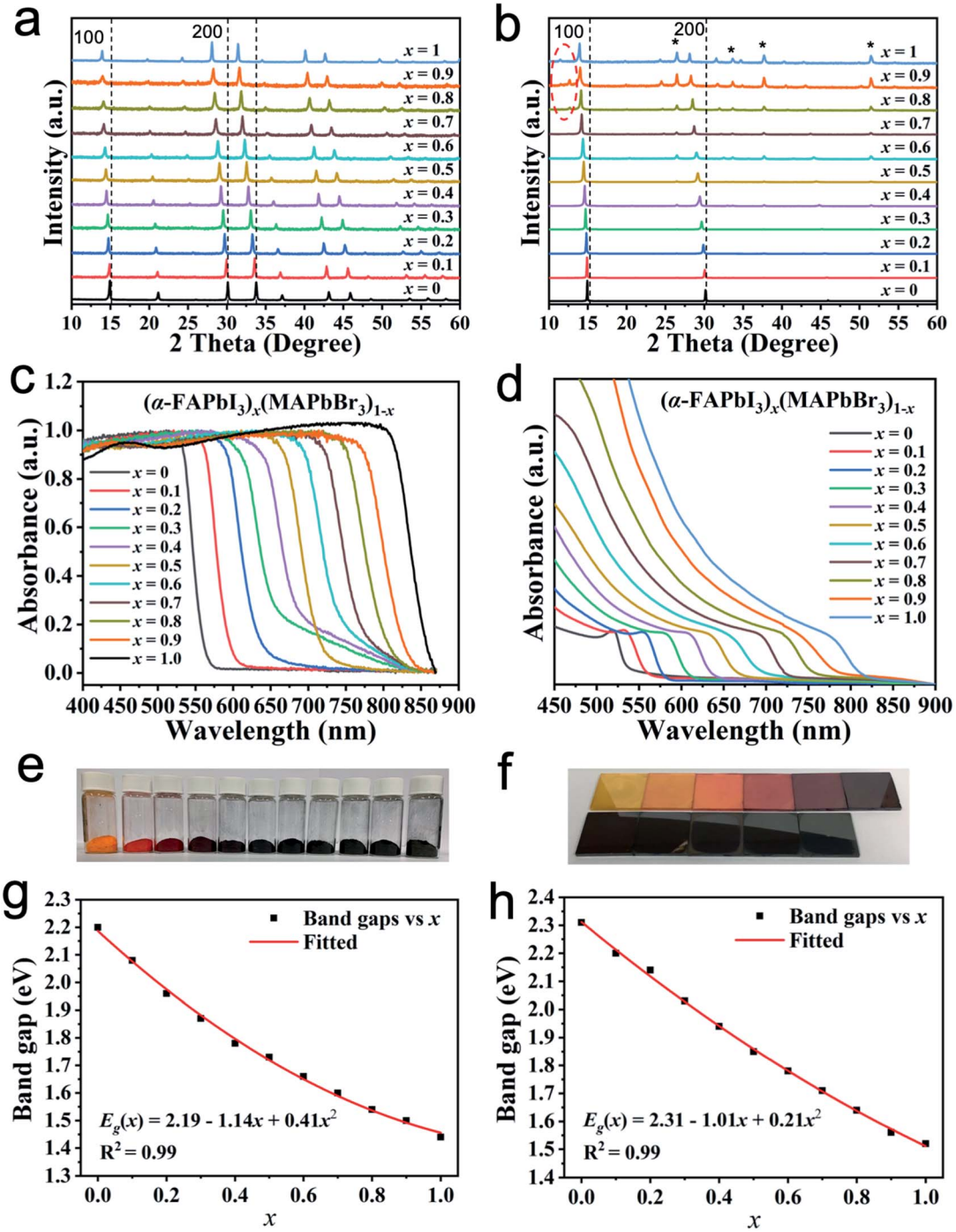


Fig. 1 XRD, UV-vis absorption spectra and photographs of $(\alpha\text{-FAPbI}_3)_x(\text{MAPbBr}_3)_{1-x}$ ($0 \leq x \leq 1$) perovskites. XRD patterns of (a) powders prepared by MCS and (b) films prepared by SS; the reflections of the FTO substrates are labelled with "*"; UV-vis absorption spectra of (c) powders prepared by MCS and (d) films prepared by SS; photographs of (e) powders and (f) films on the mp-$TiO_2$/bl-$TiO_2$/FTO substrates (top: $x = 0$, 0.1, …, 0.5; down: $x = 0.6$, …, 1.0); quadratic relationship of the band gaps of $(\alpha\text{-FAPbI}_3)_x(\text{MAPbBr}_3)_{1-x}$ as a function of the $\alpha$-$FAPbI_3$ composition ($x$), (g) powders and (h) films.

To investigate the elemental composition and distribution of $(\alpha\text{-FAPbI}_3)_x(\text{MAPbBr}_3)_{1-x}$ powders and films, energy dispersive X-ray (EDX) elemental mapping was performed (Fig. S3 and S4, ESI†). The EDX spectra demonstrates that all the elements contained in the perovskites (*i.e.* N, Pb, I and Br) are evenly distributed in powders and films. The detailed quantitative results are summarised (Table S1, ESI†). The atomic percentage of $(\alpha\text{-FAPbI}_3)_x(\text{MAPbBr}_3)_{1-x}$ powders follows the desired stoichiometry more closely than that of films, thereby demonstrating that a fine control over composition is possible through MCS. However, a small deviation in composition may be caused

by incomplete/partial reaction in the corner area of the grinding vial or measurement errors.

Fig. 1d shows the UV-vis absorption of $(\alpha\text{-FAPbI}_3)_x(\text{MAPbBr}_3)_{1-x}$ films prepared by SS on the mp-$TiO_2$/bl-$TiO_2$/FTO substrates. A progressive blue shift in the absorption edge immediately occurred with the same $x$ ratio compared with that by MCS, which means that the band gap energy of powders is less than that of the films. Hence, the sample synthesised according to the MCS route showed a more efficient band gap energy than that processed *via* the traditional SS method. A small band gap energy corresponds to a wide light absorption range that will be beneficial for solar cells and many other optoelectronics. The absorption onsets and band gaps for both samples are listed in detail (Table S2, ESI†). Fig. 1f shows the corresponding colours of $(\alpha\text{-FAPbI}_3)_x(\text{MAPbBr}_3)_{1-x}$ films consistent with those of powders. A least-squares fit (red line) of $E_g$ in Fig. 1h is also provided. The bowing parameter ($b = 0.21$ eV) is much smaller than 0.41 eV, which indicates that the $(\alpha\text{-FAPbI}_3)_x(\text{MAPbBr}_3)_{1-x}$ prepared by the SS route has a better miscibility than that by the MCS route.

Furthermore, $(\delta\text{-FAPbI}_3)_x(\text{MAPbBr}_3)_{1-x}$ perovskites powders were also prepared by MCS. The XRD patterns indicate that all perovskites consist of a cubic structure with diffraction peak positions shifting to lower $2\theta$ values with increasing δ-$FAPbI_3$ content in the $x$ range of 0–0.8 (Fig. S5a, ESI†). Phase segregation was observed when $x = 0.9$. The residual impurities belong to δ-$FAPbI_3$ ($2\theta$, ~11.6°). We also measured the UV-vis absorption spectra of $(\delta\text{-FAPbI}_3)_x(\text{MAPbBr}_3)_{1-x}$ powders (Fig. S5b, ESI†). A systematic shift in the absorption band edge to a longer wavelength with increasing δ-$FAPbI_3$ content in $(\delta\text{-FAPbI}_3)_x(\text{MAPbBr}_3)_{1-x}$ still exists except for δ-$FAPbI_3$. The absorption onsets and band gaps are listed in detail (Table S3, ESI†).

To examine the thermal stability of the perovskites, thermogravimetric analysis (TGA) was carried out under nitrogen flow from RT to 600 °C (Fig. S6, ESI†). The TGA-DSC measurements show that perovskites decomposed before melting at the temperature range of 226–300 °C for $(\alpha\text{-FAPbI}_3)_x(\text{MAPbBr}_3)_{1-x}$ and $(\delta\text{-FAPbI}_3)_x(\text{MAPbBr}_3)_{1-x}$ prepared by MCS with good thermal stability (Table S4, ESI†). The decomposition temperature also gradually increases with the increase in $FAPbI_3$ content, thereby indicating that $FAPbI_3$ can increase the thermal stability of perovskites, which is good for device stability based on $(\text{FAPbI}_3)_x(\text{MAPbBr}_3)_{1-x}$.

The $(\text{FAPbI}_3)_{0.95}(\text{MAPbBr}_3)_{0.05}$ perovskite is a widely used perovskite for high efficiency solar cells because of its wide light absorption range from 400 nm to 850 nm and the stabilisation of α-$FAPbI_3$ can be achieved by mixing a small amount of $MAPbBr_3$. Pure phase $(\alpha\text{-FAPbI}_3)_{0.95}(\text{MAPbBr}_3)_{0.05}$ was chosen to fabricate solution-processed PSCs to evaluate the photovoltaic performance of mixed-cation/anion $(\alpha\text{-FAPbI}_3)_x(\text{MAPbBr}_3)_{1-x}$ perovskites. The reference material $(\alpha\text{-FAPbI}_3)_{0.95}(\text{MAPbBr}_3)_{0.05}$ was also synthesised from the direct SS method between FAI, $PbI_2$, MABr and $PbBr_2$ in the corresponding ratio for comparison (see the Experimental section for further details). To check the quality of the $(\alpha\text{-FAPbI}_3)_{0.95}(\text{MAPbBr}_3)_{0.05}$ thin films, we firstly characterised the crystal structure properties by XRD. In Fig. 2a, the crystal structures of the double cation/anion perovskite $(\alpha\text{-FAPbI}_3)_{0.95}(\text{MAPbBr}_3)_{0.05}$ powder and films (BM and SS) are cubic at RT. The δ-phase of $FAPbI_3$ was not observed confirmed the presence of pure phase α-$FAPbI_3$. Only the relative intensities of the XRD peaks of perovskites synthesised through different routes are slightly different. In powder, the intensity of (200) peak is stronger than that of (100) peak. Meanwhile, the intensity of (100) peak is stronger than that of (200) peak in films. The UV-vis absorption was recorded for perovskite powder and films (BM and SS) prepared on the mp-$TiO_2$/bl-$TiO_2$/FTO substrates to investigate optical properties. Fig. 2b shows the absorption spectra for the perovskites. The absorption edge of films shifted to a short wavelength, indicating the increasement of the band gap. The absorption onsets and band gaps of both samples are listed in Table 1. The morphological properties were also checked. The top-view SEM images of the perovskite films clearly show the compact and smooth surface coverage, and the particles exhibit diameters from 200 nm to 800 nm (BM, Fig. 2c and d) and 200 nm to1 μm (SS, Fig. 2f and g). We used the thin films for solar cell fabrication by using a stack of glass/FTO/bl-$TiO_2$/mp-$TiO_2$/perovskite/Spiro-OMeTAD/Au. The cross-sectional SEM images of the as-fabricated $(\alpha\text{-FAPbI}_3)_{0.95}(\text{MAPbBr}_3)_{0.05}$ PSCs in Fig. 2e and h show a 150 nm thick mp-$TiO_2$ layer, a 400 nm thick perovskite layer and a 200 nm thick hole transport layer.

We examined the photovoltaic performance of the devices by measuring their current–voltage ($J$–$V$) curves and their incident-photon-to-current conversion efficiency (IPCE). All the devices fabricated from the MCS powders show a higher PCE than those prepared from SS method. Fig. 3a shows representative $J$–$V$ curves of PSCs made from the MCS powders, with a PCE of 15.9% (forward scan, $V_{oc}$, $J_{sc}$ and FF being 1.02 V, 24.0 mA $cm^{-2}$ and 0.65, respectively) and 14.7% (backward scan, $V_{oc}$, $J_{sc}$ and FF being 1.04 V, 23.9 mA $cm^{-2}$ and 0.59, respectively). Fig. S7a (ESI)† shows representative $J$–$V$ curves of PSCs made from SS method, with a PCE of 15.2% (forward scan, $V_{oc}$, $J_{sc}$ and FF being 1.03 V, 25.0 mA $cm^{-2}$ and 0.59, respectively) and 15.1% (backward scan, $V_{oc}$, $J_{sc}$ and FF being 1.06 V, 24.9 mA $cm^{-2}$ and 0.57, respectively). Both devices show strong hysteresis. The IPCE spectrum demonstrates a high photon-to-current conversion efficiency from 400 nm to 800 nm. The integration of the IPCE over the AM 1.5 G spectrum yields a photocurrent density of 22.6 mA $cm^{-2}$ (Fig. 3b), which is close to the short circuit photocurrent density of 23.9 mA $cm^{-2}$ derived from the $J$–$V$ curve. Under the optimal conditions, the power conversion efficiency distributions of the obtained devices are shown in Fig. 3c (backward scan) and Fig. 3d (forward scan). The PCE distribution is 10–16% for both scans. The average PCEs are 12.9% (backward scan) and 13.7% (forward scan). The stabilised maximum power output measurements presented in Fig. 3e and f show good agreement between the measured PCE and the power output. When applying a constant voltage of 0.77 V corresponding to the maximum power point (MMP), the output current density is stable at 20.0 mA $cm^{-2}$ under the continuous output test for 120 s, and the corresponding power conversion efficiency is 15.4%, thereby showing good continuous output stability. In the SS method, the integrated $J_{sc}$ value is 23.2 mA $cm^{-2}$ (Fig. S7b, ESI†). The efficiency distributions of

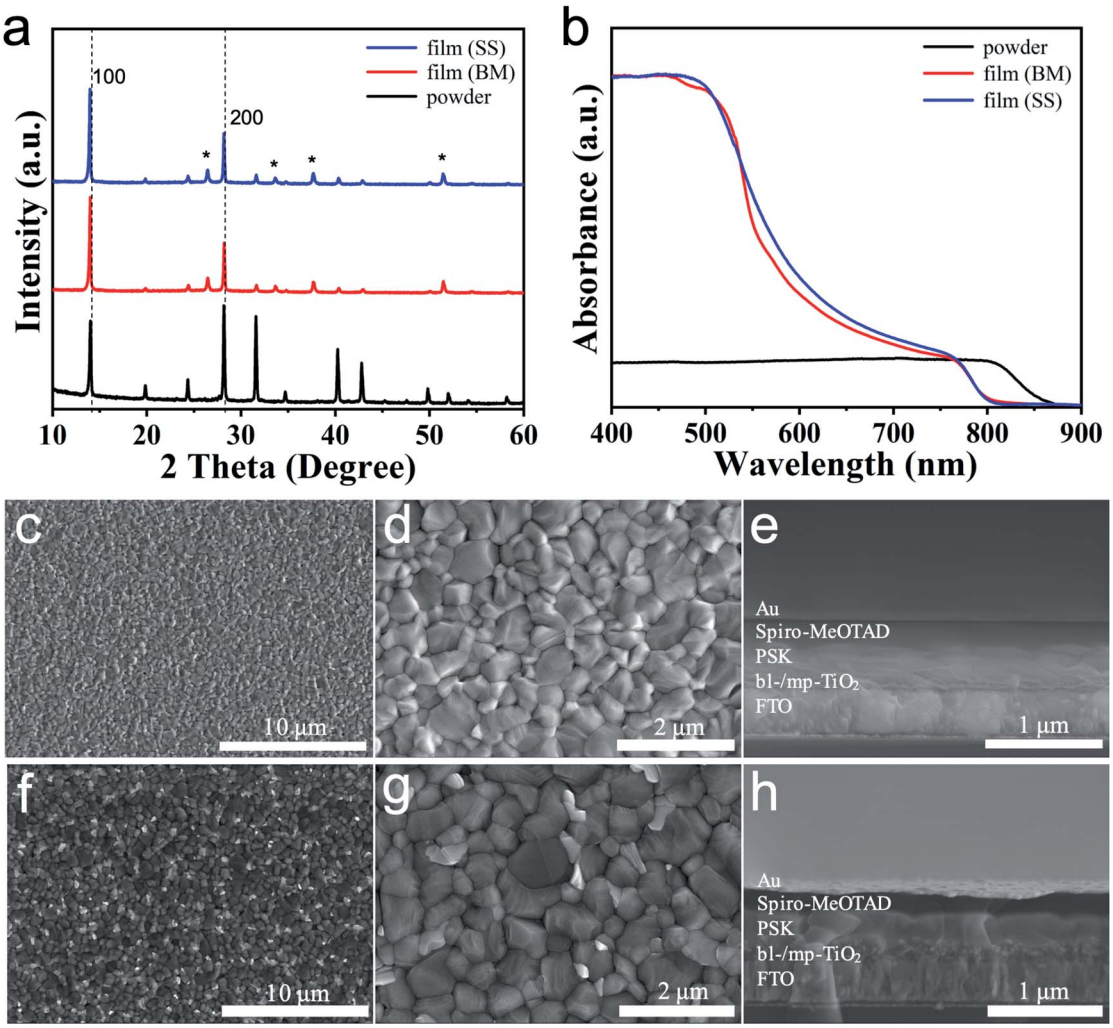


Fig. 2 (a) XRD patterns and (b) UV-vis absorption spectra of mixed-cation/anion $(\alpha\text{-}FAPbI_3)_{0.95}(MAPbBr_3)_{0.05}$ powders prepared by MCS and films (BM and SS) prepared on the mp-$TiO_2$/bl-$TiO_2$/FTO substrates; the reflections of the FTO substrates are labelled with "*"; SEM images, including the top and cross-sectional views of the $(\alpha\text{-}FAPbI_3)_{0.95}(MAPbBr_3)_{0.05}$ films, (c–e) BM and (f–h) SS.

Table 1 Optical properties of $(\alpha\text{-}FAPbI_3)_x(MAPbBr_3)_{1-x}$ powders and films

| $(\alpha\text{-}FAPbI_3)_{0.95}(MAPbBr_3)_{0.05}$ | Powder | Film (BM) | Film (SS) |
|---|---|---|---|
| $\lambda_{onset}$ (nm) | 860 | 802 | 801 |
| $E_g$ (eV) | 1.44 | 1.55 | 1.55 |

the obtained devices are shown in Fig. S7c and d.† The steady-state output measurements presented in Fig. S7e and f† also show good continuous output stability (see the ESI† for further details).

Furthermore, we explored the incorporation of $K^+$ into the perovskites by MCS. Pure phase $(KPbI_3)_{0.05}(FAPbI_3)_{0.9}(MAPbBr_3)_{0.05}$ was chosen to fabricate solution-processed PSCs. The reference material $(KPbI_3)_{0.05}(FAPbI_3)_{0.9}(MAPbBr_3)_{0.05}$ was also synthesised from the direct SS method for comparison (see the Experimental section for further details). XRD analysis was performed to investigate the effect of incorporating $K^+$ into the perovskite. In Fig. 4a, the crystal structures of the mixed-cation/anion perovskite $(KPbI_3)_{0.05}(FAPbI_3)_{0.9}(MAPbBr_3)_{0.05}$ powder and films (BM and SS) are cubic at RT. The XRD peaks were shifted to a small angle when the 5% $K^+$ was incorporated compared with $(\alpha\text{-}FAPbI_3)_{0.95}(MAPbBr_3)_{0.05}$, indicating the elongation of crystal lattice. Considering Goldschmidt's tolerance factor, the perovskite containing small cations would be collapsed. However, the $K^+$-doped perovskite structure was kept as the cubic for a ratio of 5% $K^+$, suggesting that the $K^+$ was homogeneously incorporated into the crystal structure. The δ-phase of $FAPbI_3$ was not observed for powder and films (BM). However, the diffraction pattern of the films prepared from the SS method shows a weak peak at ~11.6° that correspond to the δ-$FAPbI_3$. Thus, the presence of the yellow δ-$FAPbI_3$ phase might cause lower photovoltaic performance compared with the PSCs fabricated with powder. Only the relative intensities of the XRD peaks of perovskites synthesised through different routes vary. The UV-vis absorption was recorded for perovskite prepared on

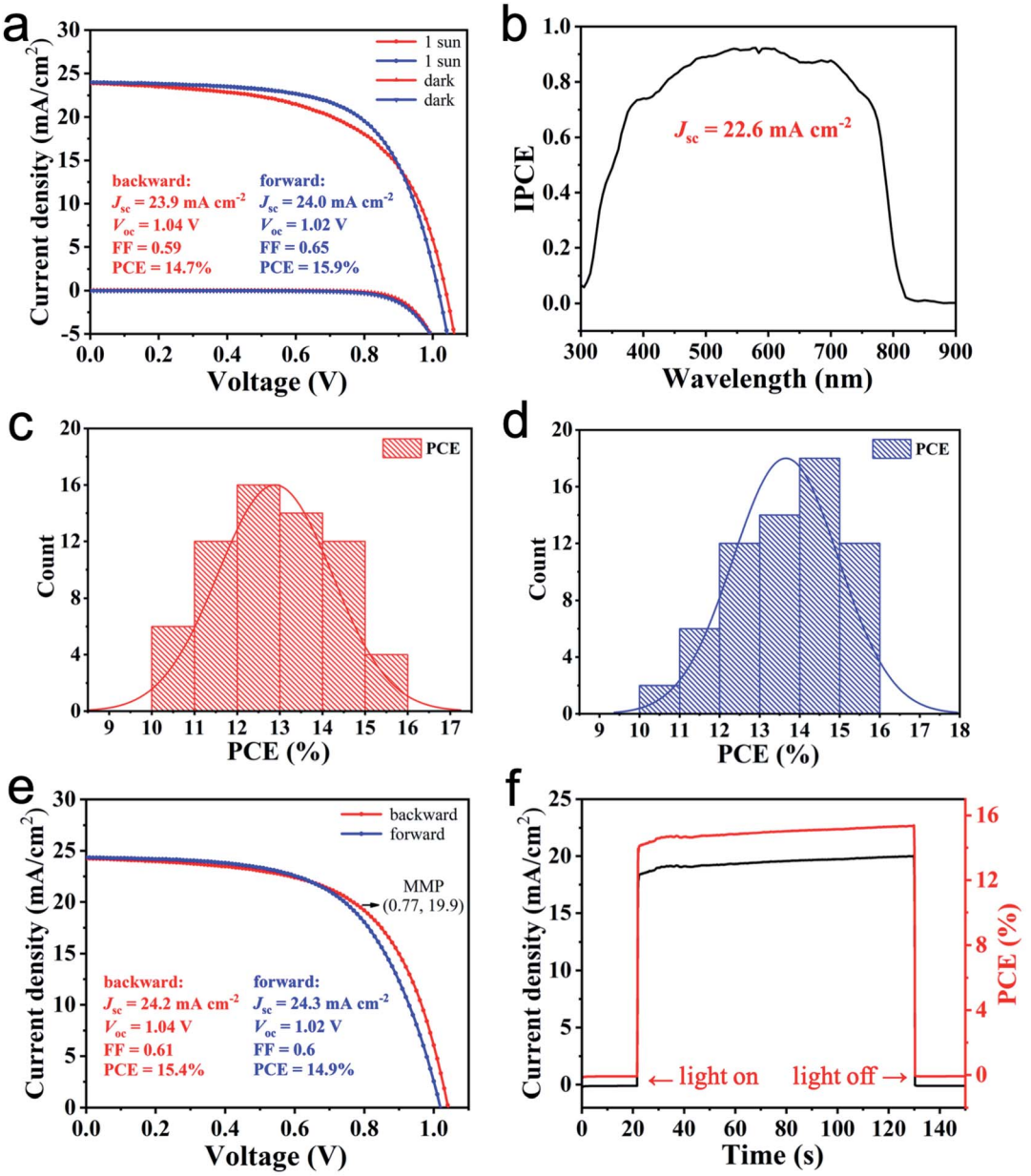


Fig. 3 (a) $J$–$V$ curves of the best performing cell under forward and backward scans by using $(\alpha\text{-FAPbI}_3)_{0.95}(\text{MAPbBr}_3)_{0.05}$ perovskite prepared by MCS; (b) IPCE test result and integrated $J_{sc}$ value; cell efficiency distributions; (c) backward scan; (d) forward scan; (e) $J$–$V$ curves of the cell for steady-state output test; (f) steady-state current density and PCE continuous output of the tested cell at MMP for 120 s.

mp-$TiO_2$/bl-$TiO_2$/FTO substrates to investigate the effect of $K^+$ incorporation on the optical properties. Fig. 4b shows the absorption spectra for the perovskite with 5% $K^+$. The absorption edge of powder shifted to a longer wavelength than films, indicating the reduction of the band gap. The absorption onsets and band gaps for both samples are listed in Table 2. The band gaps of the perovskites remain unchanged with 5% $K^+$ ratio compared with those of $(\alpha\text{-FAPbI}_3)_{0.95}(\text{MAPbBr}_3)_{0.05}$. The effect of $K^+$ on the morphology of the perovskite was investigated by SEM analysis. The surface SEM images for perovskite films with 5% $K^+$ ratio are shown in Fig. 4c and d (BM) and Fig. 4f and g (SS), and the corresponding cross-sectional SEM images are shown in Fig. 4e (BM) and Fig. 4h (SS). The top-view images show that the grains are tightly stacked and become a little smaller with the incorporation of 5% $K^+$ compared with those of $(\alpha\text{-FAPbI}_3)_{0.95}(\text{MAPbBr}_3)_{0.05}$. The top-view images reveal the compact and smooth morphology of the perovskite capping layer, which is formed by 200–1000 nm-sized (BM) and 150–900 nm-sized (SS) densely packed grains without voids, respectively. The dense structure of the capping layer is also confirmed by the SEM cross-sectional images of the whole device shown in Fig. 4e (BM) and Fig. 4h (SS). The cross-sectional SEM images of the as-fabricated $(\text{KPbI}_3)_{0.05}(\text{FAPbI}_3)_{0.9}(\text{MAPbBr}_3)_{0.05}$ PSCs show a 150 nm thick mp-$TiO_2$ layer, a 400 nm thick perovskite layer

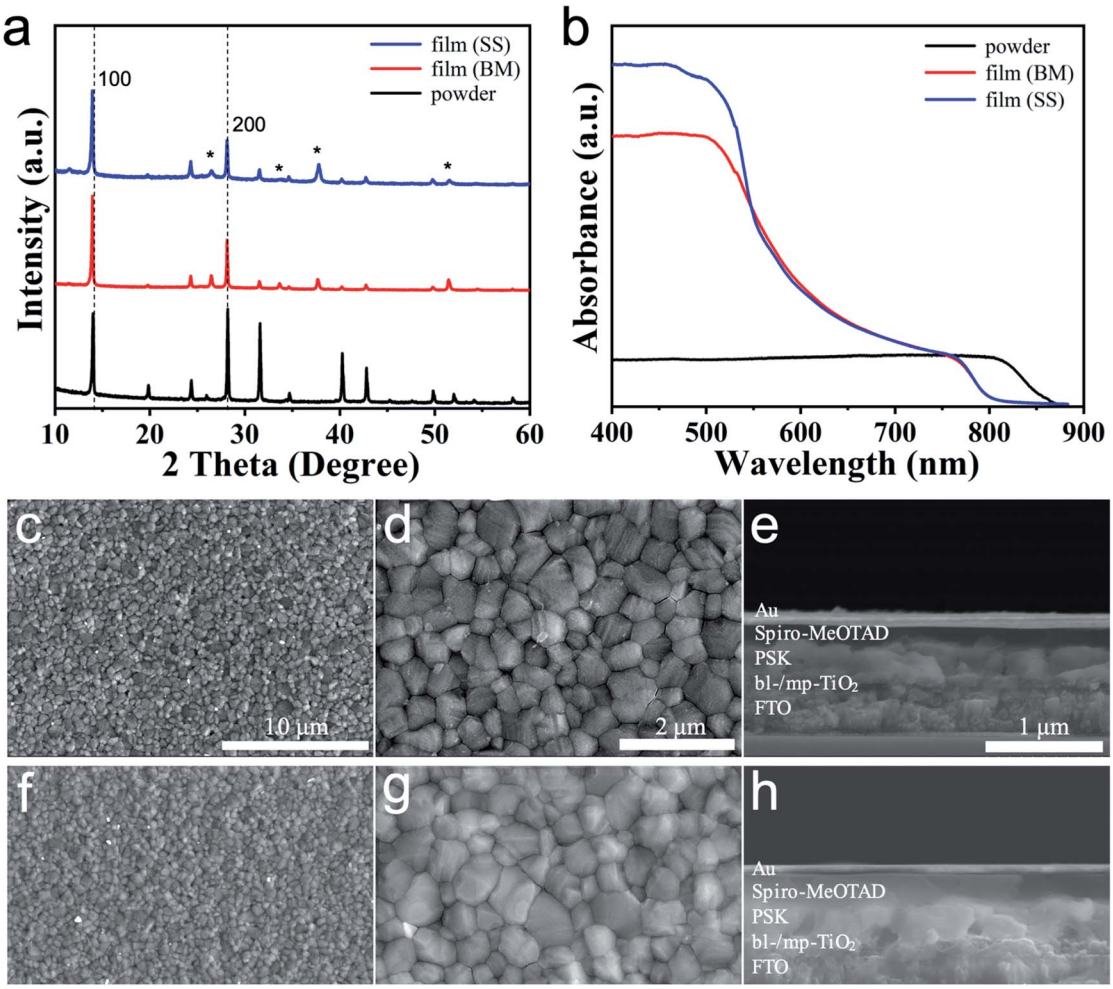


Fig. 4 (a) XRD patterns and (b) UV-vis absorption spectra of mixed-cation/anion $(KPbI_3)_{0.05}(FAPbI_3)_{0.9}(MAPbBr_3)_{0.05}$ powders prepared by MCS and films (BM and SS); the reflections of the FTO substrates are labelled with "*"; SEM images, including top and cross-sectional views of the $(KPbI_3)_{0.05}(FAPbI_3)_{0.9}(MAPbBr_3)_{0.05}$ films, (c–e) BM and (f–h) SS.

Table 2 Optical properties of $(KPbI_3)_{0.05}(FAPbI_3)_x(MAPbBr_3)_{1-x}$ powders and films

| $(KPbI_3)_{0.05}(FAPbI_3)_{0.9}(MAPbBr_3)_{0.05}$ | Powder | Film (BM) | Film (SS) |
|---|---|---|---|
| $\lambda_{onset}$ (nm) | 865 | 803 | 803 |
| $E_g$ (eV) | 1.43 | 1.55 | 1.55 |

and a 200 nm thick hole transport layer. In the cross-sectional SEM images, there are no horizontal grain boundaries for 5% $K^+$-doped perovskite absorber, whereas horizontal grain boundaries are apparent at the middle of $(\alpha\text{-}FAPbI_3)_{0.95}(MAPbBr_3)_{0.05}$ perovskite layer without $K^+$. The structure without horizontal grain boundaries would be favourable for carrier diffusion and superior photovoltaic performance.

EDX elemental mapping was performed to investigate the elemental composition and distribution of $(KPbI_3)_{0.05}(FAPbI_3)_{0.9}(MAPbBr_3)_{0.05}$ perovskite film (BM). EDX spectroscopy from the top (Fig. 5) and cross-sectional views (Fig. S8, ESI†) demonstrate that all the elements contained in the perovskite (*i.e.* K, Pb, I and Br) are evenly distributed in the film (surface and bulk). However, the K content is relatively high in both films (BM and SS) because EDX is a semi-quantitative test method with measurement errors (Fig. S9 and S10, ESI†).

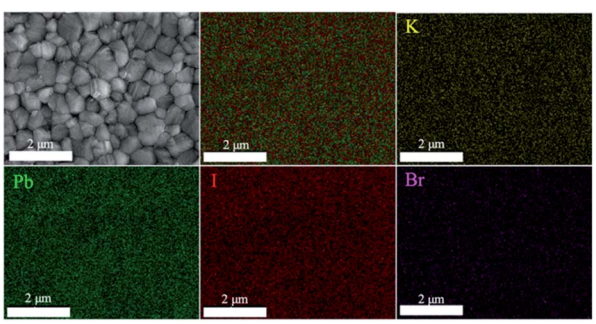


Fig. 5 SEM top-view and EDX elemental mapping images demonstrate the homogeneous distribution of K, Pb, I and Br in the $(KPbI_3)_{0.05}(FAPbI_3)_{0.9}(MAPbBr_3)_{0.05}$ film (BM).

PSCs with a mesoporous structure of glass/FTO/bl-$TiO_2$/mp-$TiO_2$/perovskite/Spiro-OMeTAD/Au were fabricated to investigate the influence of the $K^+$ incorporation. All the devices fabricated from the MCS powders show a higher PCE than those prepared from the SS method. Fig. 6a shows representative *J–V* curves of PSCs made from the MCS powders with 5% $K^+$, with a PCE of 16.7% (forward scan, $V_{oc}$, $J_{sc}$ and FF being 1.04 V, 25.0 mA $cm^{-2}$ and 0.64, respectively) and 16.2% (backward scan, $V_{oc}$, $J_{sc}$ and FF being 1.06 V, 25.1 mA $cm^{-2}$ and 0.61, respectively). Importantly, the hysteresis between the forward and the backward scan is negligible. Fig. S11a (ESI)† shows representative *J–V* curves of PSCs made from the SS method, with a PCE of 14.5% (forward scan, $V_{oc}$, $J_{sc}$ and FF being 1.0 V, 24.4 mA $cm^{-2}$ and 0.59, respectively) and 15.1% (backward scan, $V_{oc}$, $J_{sc}$ and FF being 1.02 V, 24.6 mA $cm^{-2}$ and 0.6, respectively). As mentioned above, the residual yellow δ-$FAPbI_3$ resulted in the formation of lattice defects, which would lower the photovoltaic performance of the PSCs. The IPCE spectrum demonstrates a high photon-to-current conversion efficiency from 400 nm to 800 nm. The integrated current density (23.3 mA $cm^{-2}$) obtained from the IPCE spectrum (AM 1.5 G) is well matched to the value (25.0 mA $cm^{-2}$) measured from the *J–V* curves (Fig. 6b). Under the

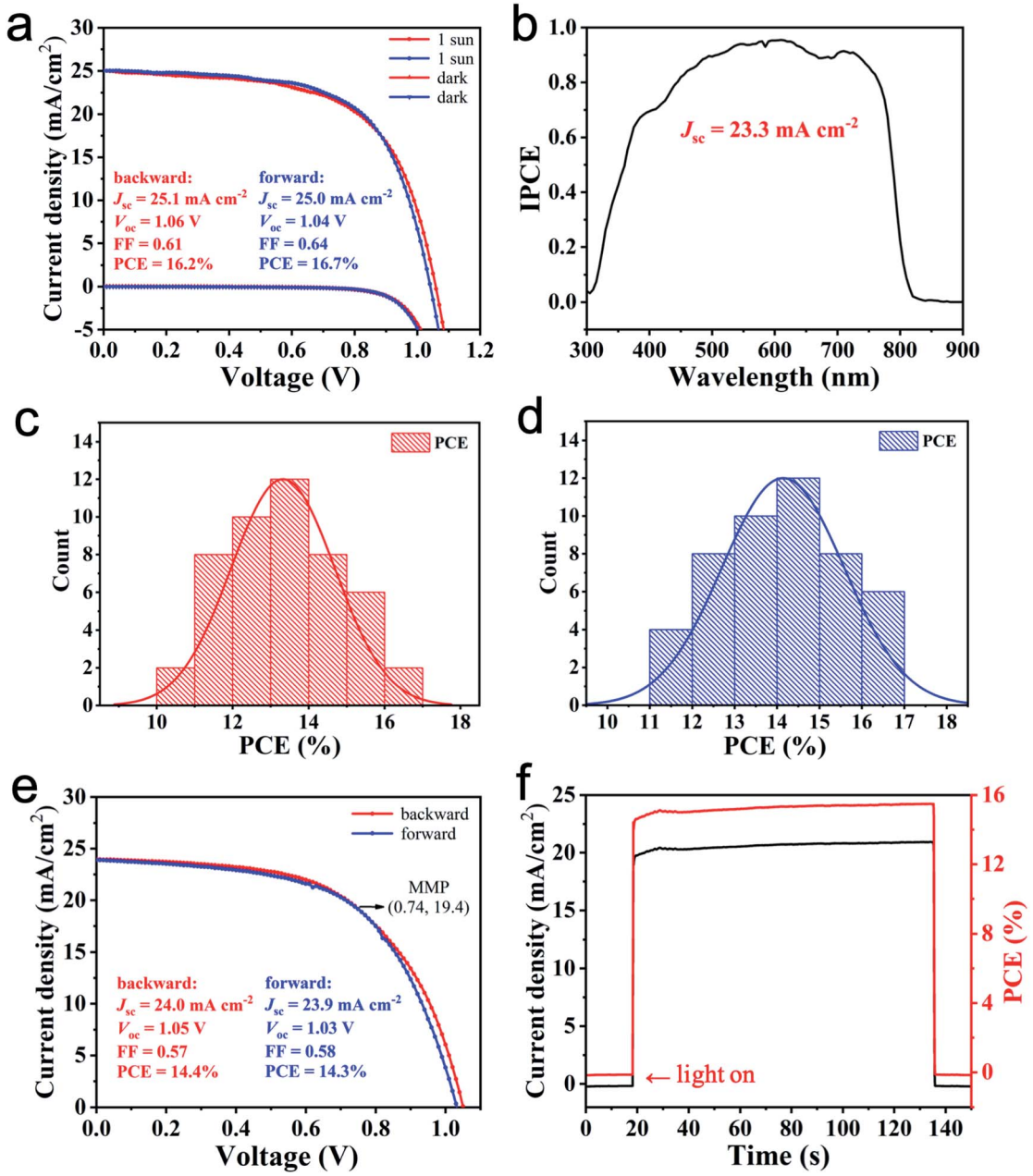


Fig. 6 (a) *J–V* curves of the best performing cell under forward and backward scans by using $(KPbI_3)_{0.05}(FAPbI_3)_{0.9}(MAPbBr_3)_{0.05}$ perovskite prepared by MCS; (b) IPCE test result and integrated $J_{sc}$ value; cell efficiency distributions; (c) backward scan; (d) forward scan; (e) *J–V* curves of the cell for steady-state output test; (f) steady-state current density and PCE continuous output of the tested cell at MMP for 120 s.

optimal conditions, the power conversion efficiency distributions of the obtained devices are shown in Fig. 6c (backward scan) and Fig. 6d (forward scan). The obtained devices have relatively narrow efficiency distributions, which proves that the method has good repeatability. The PCE distribution is 11–17% for both scans. The average PCEs are 13.3% (backward scan) and 14.2% (forward scan). The stabilised maximum power output measurements presented in Fig. 6e and f show good agreement between the measured PCE and the power output. When applying a constant voltage of 0.74 V corresponding to the MMP, the output current density is stable at 20.5 mA $cm^{-2}$ under the continuous output test for 120 s, and the corresponding power conversion efficiency is 15.2%, thus showing good continuous output stability. The maximum photovoltaic performance was increased at the 5% $K^+$ ratio. In the SS method, the integrated $J_{sc}$ value is 22.8 mA $cm^{-2}$ (Fig. S11b, ESI†). The efficiency distributions of the obtained devices are shown in Fig. S11c and d.† The steady-state output measurements presented in Fig. S11e and f† also show good continuous output stability (see the ESI† for further details).

The TGA curve shows the thermal stability of $(KPbI_3)_{0.05}(FAPbI_3)_{0.9}(MAPbBr_3)_{0.05}$ powders prepared by MCS (Fig. S10†). It decomposed at 278 °C, which is a bit lower than that of $(\alpha\text{-}FAPbI_3)_{0.95}(MAPbBr_3)_{0.05}$ ($T_d$: ~285 °C) because of less $FAPbI_3$ content as previously discussed.

## Conclusions

In conclusion, we have demonstrated the MCS route as an efficient strategy for the preparation of pure phase mixed-cation/anion $(\alpha\text{-}FAPbI_3)_x(MAPbBr_3)_{1-x}$ ($0 \leq x \leq 1$) hybrid perovskites. The stabilisation of a structurally stable $\alpha$-$FAPbI_3$ perovskite was achieved by fine and controllable compositional engineering. Thus, the optical band gaps can be easily tuned by compositional control. The newly synthesised $(\alpha\text{-}FAPbI_3)_{0.95}(MAPbBr_3)_{0.05}$ perovskite powder was used for PSCs fabrication and showed an impressive high PCE of 15.9% from a current–voltage ($J$–$V$) scan, which stabilises at 15.4% after 120 s of MMP output. Furthermore, the PSCs based on $(KPbI_3)_{0.05}(FAPbI_3)_{0.9}(MAPbBr_3)_{0.05}$ perovskite prepared by MCS exhibit higher photovoltaic performance and lower hysteresis compared with $(\alpha\text{-}FAPbI_3)_{0.95}(MAPbBr_3)_{0.05}$ with a maximum PCE of 16.7%. Moreover, we found that the resultant PSCs showed better photovoltaic performance compared with a conventional solution processed device. We believe that this MCS method could provide new chances to the efficient synthesis of hybrid perovskites and a promising strategy for the high-performance PSCs and many other devices. Accordingly, further studies are in progress.

## Experimental section

### Materials

Formamidine acetate ($NH_2CH{=}NH{\cdot}CH_3COOH$) (99.0%), methylamine ($CH_3NH_2$) (40.0 wt% in ethanol), hydrobromide acid (HBr) (48.0 wt% in water), hydroiodic acid (HI) (45.0–50.0 wt% in water, stable with 1.5 wt% hypophosphorous) and KI (99.0%) were purchased from Aladdin Reagent Ltd. (China). $PbBr_2$ (99.0%) and $PbI_2$ (99.0%) were purchased from Macklin Reagent Ltd. (China). $CH_3NH_3Cl$ (99.0%) and other basic materials were purchased from Shanghai Reagent Ltd. (China). All materials were used as received without further purification.

### Synthetic procedures

**Synthesis of $CH_3NH_3Br$.** $CH_3NH_3Br$ was synthesised by mixing $CH_3NH_2$ and HBr with the molar ratio of 1.2 : 1. HBr was dropwise added into the $CH_3NH_2$ solution in a flask under nitrogen atmosphere in an iced bath for 2 h. The resulting solution was evaporated at 55 °C in a rotary evaporator for approximately 2 h to remove the solvent. The white $CH_3NH_3Br$ crystalline powders were collected *via* Büchner funnel filtration after being washed thrice with anhydrous ethanol, recrystallised in anhydrous diethyl ether and dried in a vacuum oven at 60 °C overnight.

**Synthesis of $NH_2CH{=}NH_2I$.** $NH_2CH{=}NH_2I$ was synthesised with the same procedure as above except by replacing $CH_3NH_2$ and HBr with $NH_2CH{=}NH$ and HI.

**Synthesis of $MAPbBr_3$.** $MAPbBr_3$ powders were synthesised by mixing the desired amount of $CH_3NH_3Br$ with $PbBr_2$ (1 : 1 n/n, molar ratio) in an agate jar and reacted *via* mechanical BM (planetary ball mill, Nanjing University, QM-3SP04) at RT under ambient condition (speed, 300 rpm; humidity, ~20%).

**Synthesis of $FAPbI_3$.** δ-$FAPbI_3$ powders were synthesised with the same procedure as $MAPbBr_3$ except by replacing $CH_3NH_3Br$ and $PbBr_2$ with $NH_2CH{=}NH_2I$ and $PbI_2$. α-$FAPbI_3$ powders were obtained by sintering δ-$FAPbI_3$ at 160 °C for 60 min.

**Synthesis of $(\alpha\text{-}FAPbI_3)_x(MAPbBr_3)_{1-x}$ and $(\delta\text{-}FAPbI_3)_x(MAPbBr_3)_{1-x}$ ($0 \leq x \leq 1$) powders.** $(\alpha\text{-}FAPbI_3)_x(MAPbBr_3)_{1-x}$ powders were synthesised by mixing a desired amount of α-$FAPbI_3$ with $MAPbBr_3$ in an agate jar and reacted *via* mechanical BM for 3 h at RT under ambient condition (speed, 300 rpm; humidity, ~20%). $(\delta\text{-}FAPbI_3)_x(MAPbBr_3)_{1-x}$ powders were synthesised with the same procedure as above except by replacing α-$FAPbI_3$ with δ-$FAPbI_3$.

**Synthesis of $(KPbI_3)_{0.05}(FAPbI_3)_{0.9}(MAPbBr_3)_{0.05}$ powders.** $(KPbI_3)_{0.05}(FAPbI_3)_{0.9}(MAPbBr_3)_{0.05}$ powders were synthesised by mixing 0.05 mmol KI and 0.05 mmol $PbI_2$ with 0.9 mmol α-$FAPbI_3$ and 0.05 mmol $MAPbBr_3$ in an agate jar and reacted *via* mechanical BM for 3 h at RT under ambient condition (speed, 300 rpm; humidity, ~20%).

### Preparation of $(\alpha\text{-}FAPbI_3)_x(MAPbBr_3)_{1-x}$ ($0 \leq x \leq 1$) films

A dense blocking layer of $TiO_2$ (50 nm, bl-$TiO_2$) was deposited onto the FTO substrate. The FTO substrate pretreated with UV ozone for 45 min was treated with an acidic ethanol solution containing tetrabutyl titanate (Sigma-Aldrich) by spin-coating at 2000 rpm for 45 s, followed by sintering at 500 °C for 30 min. The mesoporous $TiO_2$ (mp-$TiO_2$) film was then spin coated onto the bl-$TiO_2$/FTO substrate by using diluted commercial paste (Dyesol DSL 18NR-T in ethanol, 1 : 6.5 w/w) and calcined at 500 °C for 1 h in air to remove the organic portion. The perovskite solution was prepared by dissolving 1.4 mmol $(\alpha\text{-}FAPbI_3)_x(MAPbBr_3)_{1-x}$ powders in 1 ml of DMF/DMSO (8 : 1 v/v)

mixed solvent. The perovskite precursor solution ($C = 1.4$ M) was dropped onto the mp-$TiO_2$/bl-$TiO_2$/FTO substrate. Then, the solution was spin-coated at 1000 and 5000 rpm for 5 and 20 s, respectively. During the second spin-coating step, 1 ml chlorobenzene was quickly poured onto the substrate. The substrate was placed on a hot stage at 150 °C for 10 min, with all operations under the protection of nitrogen.

### Solar cells fabrication

The mp-$TiO_2$/bl-$TiO_2$/FTO substrates were prepared with the same procedure as mentioned above. In the MCS route, the perovskite solution was prepared by dissolving 1.4 mmol $(\alpha\text{-}FAPbI_3)_{0.95}(MAPbBr_3)_{0.05}$ and 0.5 mmol MACl (1.4 mmol $(KPbI_3)_{0.05}(FAPbI_3)_{0.9}(MAPbBr_3)_{0.05}$ and 0.5 mmol MACl) in 1 ml of DMF/DMSO (8 : 1 v/v) mixed solvent. In the SS route, the perovskite solution was prepared by dissolving 1.33 mmol FAI, 1.33 mmol $PbI_2$, 0.07 mmol MABr, 0.07 mmol $PbBr_2$ and 0.5 mmol MACl (0.07 mmol KI, 1.26 mmol FAI, 1.33 mmol $PbI_2$, 0.07 mmol MABr, 0.07 mmol $PbBr_2$ and 0.5 mmol MACl) in 1 ml of DMF/DMSO (8 : 1 v/v) mixed solvent. The perovskite precursor solution ($C = 1.4$ M) was dropped onto the mp-$TiO_2$/bl-$TiO_2$/FTO substrate. Then, spin-coating was performed at 1000 and 5000 rpm for 5 and 20 s, respectively. During the second spin-coating step, 1 ml chlorobenzene was quickly poured onto the substrate. The substrate was placed on a hot stage at 150 °C for 10 min, with all operations under the protection of nitrogen. The hole transporting material (HTM) solution was prepared by dissolving 74 mg spiro-OMeTAD in 1 ml chlorobenzene containing 28.8 μl of 4-*tert*-butylpyridine, 9.1 mg lithium bis(trifluoromethanesulphonyl)imide and 17.5 μl acetonitrile (99.8%, Sigma-Aldrich). Subsequently, the HTM was deposited on top of the perovskite layer by spin-coating at 2000 rpm for 30 s. Device fabrication was completed by magnetron sputtering of a thin gold layer (100 nm) on top of the perovskite with the HTM. The active area is approximately 0.0314 or 0.06 $cm^{-2}$.

### Characterisation

Powder X-ray diffraction (XRD) patterns of the products were collected using a Philips X′ Pert Pro with Cu $K_{\alpha 1}$ line ($\lambda$ = 1.54186 Å) at $V = 40$ kV and $I = 40$ mA. The morphology and structure of the products were observed with a scanning electron microscope (SEM, Hitachi S-4800). Elemental mapping images were observed by EDX (EDAX Apollo). The UV-vis-NIR diffuse reflectance spectrum was measured at RT by using a UV-vis-NIR spectrophotometer (Shimadzu UV-3600 Plus) with an integrating sphere attachment operating in the 300–1200 nm region. A highly refined $BaSO_4$ powder plate was used as the standard (100% reflectance). TGA-DSC was performed on a TA Q600 SDT. The sample was placed in an $Al_2O_3$ crucible and heated in an interval from RT to 600 °C at a ramp rate of 10 °C $min^{-1}$ under flowing nitrogen gas with a flow rate of 100 ml $min^{-1}$. Approximately 5 mg of the powder was used for each experiment. The current–voltage ($J$–$V$) tests of PSCs were conducted on a Keithley Model 2000 with an AM 1.5 solar simulator (Yamashita DESO, Japan). The system was calibrated against a certified silicon solar cell, and the light intensity is 100 mW $cm^{-2}$. External quantum efficiency measurements were performed by using a solar cell monochromatic incident photon-to-electron conversion efficiency (IPCE) measurement system (SCS10-X150-DSSC, Zolix).

## Conflicts of interest

There are no conflicts to declare.

## Acknowledgements

This study is jointly supported by the National Natural Science Foundation of China (Grant No. 52073002, 51773003, and 51711540302) and National Key Research and Development Program of China (Grant No. 2020YFB1506400).

## References

1 D. Shi, V. Adinolfi, R. Comin, M. Yuan, E. Alarousu, A. Buin, Y. Chen, S. Hoogland, A. Rothenberger, K. Katsiev, Y. Losovyj, X. Zhang, P. A. Dowben, O. F. Mohammed, E. H. Sargent and O. M. Bakr, *Science*, 2015, **347**, 519.
2 C. Wehrenfennig, G. E. Eperon, M. B. Johnston, H. J. Snaith and L. M. Herz, *Adv. Mater.*, 2014, **26**, 1584.
3 S. D. Stranks, G. E. Eperon, G. Grancini, C. Menelaou, M. J. P. Alcocer, T. Leijtens, L. M. Herz, A. Petrozza and H. J. Snaith, *Science*, 2013, **342**, 341.
4 G. Xing, N. Mathews, S. Sun, S. S. Lim, Y. M. Lam, M. Grätzel, S. Mhaisalkar and T. C. Sum, *Science*, 2013, **342**, 344.
5 Q. Dong, Y. Fang, Y. Shao, P. Mulligan, J. Qiu, L. Cao and J. Huang, *Science*, 2015, **347**, 967.
6 H. Lu, Y. Liu, P. Ahlawat, A. Mishra, W. R. Tress, F. T. Eickemeyer, Y. Yang, F. Fu, Z. Wang, C. E. Avalos, B. I. Carlsen, A. Agarwalla, X. Zhang, X. Li, Y. Zhan, S. M. Zakeeruddin, L. Emsley, U. Rothlisberger, L. Zheng, A. Hagfeldt and M. Grätzel, *Science*, 2020, **370**, 74.
7 M. Jeong, I. W. Choi, E. M. Go, Y. Cho, M. Kim, B. Lee, S. Jeong, Y. Jo, H. W. Choi, J. Lee, J. H. Bae, S. K. Kwak, D. S. Kim and C. Yang, *Science*, 2020, **369**, 1615.
8 N. J. Jeon, H. Na, E. H. Jung, T.-Y. Yang, Y. G. Lee, G. Kim, H.-W. Shin, S. II Seok, J. Lee and J. Seo, *Nat. Energy*, 2018, **3**, 682.
9 N. J. Jeon, J. H. Noh, Y. C. Kim, W. S. Yang, S. Ryu and S. II Seok, *Nat. Mater.*, 2014, **13**, 897.
10 N. J. Jeon, J. H. Noh, W. S. Yang, Y. C. Kim, S. Ryu, J. Seo and S. II Seok, *Nature*, 2015, **517**, 476.
11 S. A. Kulkarni, T. Baikie, P. P. Boix, N. Yantara, N. Mathews and S. Mhaisalkar, *J. Mater. Chem. A*, 2014, **2**, 9221.
12 J. H. Noh, S. H. Im, J. H. Heo, T. N. Mandal and S. II Seok, *Nano Lett.*, 2013, **13**, 1764.
13 D. P. McMeekin, G. Sadoughi, W. Rehman, G. E. Eperon, M. Saliba, M. T. Hörantner, A. Haghighirad, N. Sakai, L. Korte, B. Rech, M. B. Johnston, L. M. Herz and H. J. Snaith, *Science*, 2016, **351**, 151.
14 M. Liu, M. B. Johnston and H. J. Snaith, *Nature*, 2013, **501**, 395.

15 Q. Chen, H. Zhou, Z. Hong, S. Luo, H.-S. Duan, H.-H. Wang, Y. Liu, G. Li and Y. Yang, *J. Am. Chem. Soc.*, 2014, **136**, 622.
16 J.-H. Im, H.-S. Kim and N.-G. Park, *APL Mater.*, 2014, **2**, 081510.
17 X. Li, D. Bi, C. Yi, J.-D. Décoppet, J. Luo, S. M. Zakeeruddin, A. Hagfeldt and M. Grätzel, *Science*, 2016, **353**, 58.
18 D.-Y. Son, S.-G. Kim, J.-Y. Seo, S.-H. Lee, H. Shin, D. Lee and N.-G. Park, *J. Am. Chem. Soc.*, 2018, **140**, 1358.
19 https://www.nrel.gov/pv/assets/pdfs/best-research-cell-efficiencies.20200925.pdf.
20 S. Tang, X. Xiao, J. Hu, B. Gao, H. Chen, Z. Peng, J. Wen, M. Era and D. Zou, *ChemPlusChem*, 2020, **85**, 240.
21 N. Pellet, P. Gao, G. Gregori, T. Yang, M. K. Nazeeruddin, J. Maier and M. Grätzel, *Angew. Chem., Int. Ed.*, 2014, **53**, 3151.
22 G. E. Eperon, S. D. Stranks, C. Menelaou, M. B. Johnston, L. M. Herz and H. J. Snaith, *Energy Environ. Sci.*, 2014, **7**, 982.
23 C. C. Stoumpos, C. D. Malliakas and M. G. Kanatzidis, *Inorg. Chem.*, 2013, **52**, 9019.
24 D. Prochowicz, P. Yadav, M. Saliba, M. Saski, S. M. Zakeeruddin, J. Lewinski and M. Grätzel, *Sustain. Energy Fuels*, 2017, **1**, 689.
25 Z. Li, M. Yang, J.-S. Park, S. Wei, J. J. Berry and K. Zhu, *Chem. Mater.*, 2016, **28**, 284.
26 M. Saliba, T. Matsui, J.-Y. Seo, K. Domanski, J.-P. C. Baena, M. K. Nazeeruddin, S. M. Zakeeruddin, W. Tress, A. Abate, A. Hagfeldtd and M. Grätzel, *Energy Environ. Sci.*, 2016, **9**, 1989.
27 H. Tan, A. Jain, O. Voznyy, X. Lan, F. P. G. Arquer, J. Z. Fan, R. Q. Bermudez, M. Yuan, B. Zhang, Y. Zhao, F. Fan, P. Li, L. N. Quan, Y. Zhao, Z. Lu, Z. Yang, S. Hoogland and E. H. Sargent, *Science*, 2017, **355**, 722.
28 Z. Tang, T. Bessho, F. Awai, T. Kinoshita, M. M. Maitani, R. Jono, T. N. Murakami, H. Wang, T. Kubo, S. Uchida and H. Segawa, *Sci. Rep.*, 2017, **7**, 12183.
29 A. M. Elseman, M. M. Rashad and A. M. Hassan, *ACS Sustainable Chem. Eng.*, 2016, **4**, 4875.
30 A. Jana, M. Mittal, A. Singla and S. Sapra, *Chem. Commun.*, 2017, **53**, 3046.
31 D. Prochowicz, M. Franckevicius, A. M. Cieslak, S. M. Zakeeruddin, M. Grätzel and J. Lewinski, *J. Mater. Chem. A*, 2015, **3**, 20772.
32 D. Prochowicz, P. Yadav, M. Saliba, M. Sasi, S. M. Zakeeruddin, J. Lewinski and M. Grätzel, *ACS Appl. Mater. Interfaces*, 2017, **9**, 28418.
33 Z. Zhu, Q. Yang, L. Gao, L. Zhang, A. Shi, C. Sun, Q. Wan and H. Zhang, *J. Phys. Chem. Lett.*, 2017, **8**, 1610.
34 N. Leupold, K. Schootz, S. Cacovich, I. Bauer, M. Schultz, M. Daubinger, L. Kaiser, A. Rebai, J. Rousset, A. Kohler, P. Schulz, R. Moos and F. Panzer, *ACS Appl. Mater. Interfaces*, 2019, **11**, 30259.
35 D. J. Kubicki, D. Prochowicz, A. Hofstetter, P. Pechy, S. M. Zakeeruddin, M. Grätzel and L. Emsley, *J. Am. Chem. Soc.*, 2017, **139**, 10055.
36 D. J. Kubicki, D. Prochowicz, A. Hofstetter, M. Saski, P. Yadav, D. Bi, N. Pellet, J. Lewinski, S. M. Zakeeruddin, M. Grätzel and L. Emsley, *J. Am. Chem. Soc.*, 2018, **140**, 3345.
37 D. Chen, J. Li, X. Chen, J. Chen and J. Zhong, *ACS Appl. Mater. Interfaces*, 2019, **11**, 10059.
38 Z. Hong, D. Tan, R. A. John, Y. K. E. Tay, Y. K. T. Ho, X. Zhao, T. C. Sum, N. Mathews, F. Garcia and H. S. Soo, *iScience*, 2019, **16**, 312.
39 M. Saski, D. Prochowicz, W. Marynowski and J. Lewinski, *Eur. J. Inorg. Chem.*, 2019, 2680.
40 A. M. Askar, A. Karmakar, G. M. Bernard, M. Ha, V. V. Terskikh, B. D. Wiltshire, S. Patel, J. Fleet, K. Shankar and V. K. Michaelis, *J. Phys. Chem. Lett.*, 2018, **9**, 2671.
41 A. Karmakar, A. M. Askar, G. M. Bernard, V. V. Terskikh, M. Ha, S. Patel, K. Shanka and V. K. Michaelis, *Chem. Mater.*, 2018, **30**, 2309.
42 B. A. Rosales, L. Men, S. D. Cady, M. P. Hanrahan, A. J. Rossini and J. Vela, *Chem. Mater.*, 2016, **28**, 6848.
43 F. Palazon, Y. E. Ajjouri and H. J. Bolink, *Adv. Energy Mater.*, 2019, 1902499.
44 B. A. Rosales, L. Wei and J. Vela, *J. Solid State Chem.*, 2019, **271**, 206.
45 M. Wang, G. T. Fei, Y. G. Zhang, M. G. Kong and L. D. Zhang, *Adv. Mater.*, 2007, **19**, 4491.
46 R. Venugopal, P. Lin and Y. Chen, *J. Phys. Chem. B*, 2006, **110**, 11691.